ACS APPLIED MATERIALS & INTERFACES

Research Article

www.acsami.org

Enhanced Therapeutic Efficacy of Doxorubicin for Breast Cancer Using Chitosan Oligosaccharide-Modified Halloysite Nanotubes

Jing Yang,[#,†] Yanping Wu,[#,‡] Yan Shen,[†] Changren Zhou,[†] Yi-Fang Li,[‡] Rong-Rong He,[*,‡] and Mingxian Liu[*,†]

[†]Department of Materials Science and Engineering and [‡]College of Pharmacy, Jinan University, Guangzhou 510632, China

Supporting Information

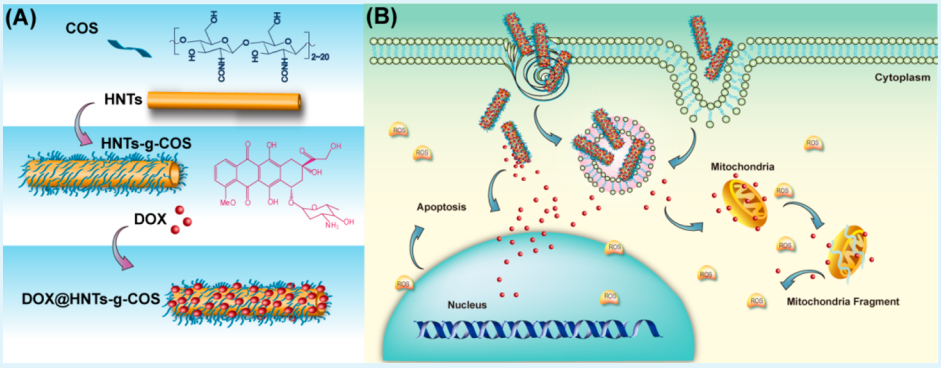

ABSTRACT: Halloysite nanotubes (HNTs) are natural aluminosilicates with unique hollow lumen structure, also having high specific area, good biocompatibility, nontoxicity, and low price. Here, we designed a chitosan oligosaccharide-grafted HNTs (HNTs-*g*-COS) as a doxorubicin (DOX) carrier for treating breast cancer both in vitro and in vivo. The structure of HNTs-*g*-COS was first characterized by various methods. HNTs-*g*-COS showed positively charged surface and improved hemocompatibility. DOX-loaded HNTs-*g*-COS (DOX@HNTs-*g*-COS) released in cell lysate in a controlled manner. The IC_{50} value of DOX@HNTs-*g*-COS toward MCF-7 cells was 1.17 μg mL^{-1}, while it was 2.43 μg mL^{-1} for free DOX. DOX@HNTs-*g*-COS increased the apoptosis effects of MCF-7 cells as shown in flow cytometry results. Also, reactive oxygen species of cells induced by DOX@HNTs-*g*-COS were drug-dose-dependent. DOX@HNTs-*g*-COS could enter the MCF-7 cells and induce mitochondrial damage as well as attack the nuclei. The in vivo antitumor effect of DOX@HNTs-*g*-COS was investigated in 4T1-bearing mice. The tumor-inhibition ratio of DOX@HNTs-*g*-COS was 83.5%, while it was 46.1% for free DOX. All mice treated with DOX@HNTs-*g*-COS survived over 60 days. DOX@HNTs-*g*-COS showed fewer ruptured cardiomyocytes and no obvious systemic toxicity. Therefore, the rational designed HNTs nanocarrier for chemotherapy drug showed promising applications in tumor treatment.

KEYWORDS: *nanotube, surface grafting, drug delivery, cell viability, tumor therapy*

1. INTRODUCTION

Cancer is the second most common cause of death in the United States and accounts for nearly 1 of every 4 deaths. According to the World Health Organization (WHO), there were 4 million new cancer cases and 8.2 million cancer-related deaths in the year of 2012 worldwide. Most human cancers are treated by surgical resection, chemotherapy, and/or radiotherapy. However, each kind of therapy has its own drawbacks. Thus, there are urgent needs and major opportunities to develop innovative technologies to treat tumors.[1] Nanotechnology can provide essential breakthroughs in the fight against cancer.[2] The core work of nanotherapy for treatment of cancer is searching effective carriers for therapeutic agents. Polymeric micelles,[3] liposomes,[4] viruses,[5] metal nanoparticles,[6] inorganic nanoparticles (including graphene oxide (GO)),[7,8] mesoporous silica,[9,10] and Fe_3O_4 nanoparticles[11] have been developed for this purpose. Drug-loaded nanocarriers can be easily uptaken by cells due to their small size, and subsequently drugs are released from the nanocarriers to kill the tumor cells or induce cell apoptosis.[12] An ideal drug nanocarrier should have high drug-loading capacity, high endocytosis efficiency, low cytotoxicity toward normal cells, good hemocompatibility, and low cost.[13,14]

Halloysite nanotubes (HNTs) are novel 1D nanomaterials which can be found to be significant applications in cancer treatment. They form in volcanic zones in the form of rolled alumosilicate sheets with a formula of $Al_2Si_2O_5(OH)_4{\cdot}nH_2O$. The external diameter, lumen, and length of HNTs vary in the range of 50−80, 10−15, and 200−1500 nm, respectively.[15−17] HNTs have many advantages as drug carriers, for example, high

Received: July 22, 2016
Accepted: September 15, 2016
Published: September 15, 2016

DOI: 10.1021/acsami.6b09074
ACS Appl. Mater. Interfaces 2016, 8, 26578−26590

Scheme 1. Schematic Illustration of the Synthesis Procedure for HNTs-*g*-COS and DOX Loading Process (A) and the Uptake Process of the DOX-Loaded Nanotubes by Cells and the Cell Apoptosis Mechanism (B)

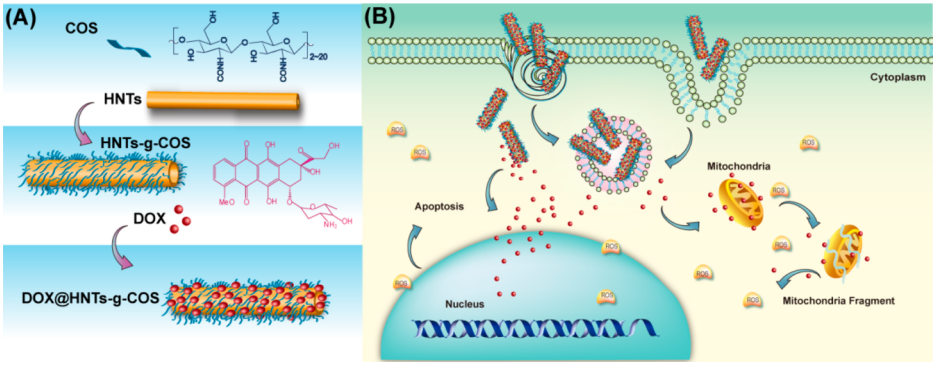

absorption ability,[18,19] high stability in biological liquid, low toxicity,[20] good biocompatibility,[21,22] low cost, and environmentally friendly.[23] HNTs contain two types of hydroxyl groups, inner and outer hydroxyl groups, which are located between layers and on the surface of the nanotubes, respectively.[24] The hydroxyl groups of HNTs provide the possibility of chemical modification for loading and releasing drugs. Silane coupling agent, synthetic polymers, biomacromolecules (chitosan, DNA, alginate, etc.), and enzymes, etc., can be grafted on HNTs to obtain functionalized nanocarriers.[25−29] The lumens of the nanotube are successfully loaded with inhibitors, flame retardant, antimicrobial agents, antioxidants, and chemotherapeutics.[30−36] Tetracycline hydrochloride was first encapsulated in the lumen of HNTs and then was electrospinned with poly(lactic-*co*-glycolic acid) (PLGA) to form drug-loaded composite fibrous mat.[37] γ-Aminopropyltriethoxysilane-functionalized HNTs were also used as carriers of antisense oligodeoxynucleotides for gene therapy.[38] Recently, we synthesized chitosan-grafted HNTs (HNTs-*g*-CS) as a nanoformulation of curcumin for enhancing anticancer efficacy.[28] All these results show that HNTs are potential nanovehicles for anticancer drug delivery in cancer therapy.

Doxorubicin (DOX) derived by chemical semisynthesis from a bacterial species, with trade name of Adriamycin, is a medication used in cancer chemotherapy.[39] The kinetics of DOX is known to interact with DNA by intercalation and to inhibit the biosynthesis of macromolecules.[40] DOX is commonly used in treatment of a wide range of cancers, including hematological malignancies (blood cancers, like leukemia and lymphoma), many types of carcinoma (solid tumors), and soft tissue sarcomas.[41] In spite of high killing ability of DOX toward cancer cells, it has obvious drawback of low selectivity of tumor cells and normal cells.[42] Therefore, the side effects of DOX are cardiotoxicity, anaphylaxis, and intracellular biochemical reactions disorder,[43,44] which limit its application.[45] DOX can enter the cell nuclei rapidly. Hence, the pathway of mitochondrial injury for tumor cell is weak.[46,47] To address the problems of DOX for tumor therapy, rational designed nanocarriers should be developed to reduce the side effects on normal cells, and enhance the anticancer efficiency via both the mitochondrial injury and nuclei injury mechanisms.[48] Previous study found that DOX-loaded hyaluronic acid-modified hydroxyapatite (HAP) could be retained in cell cytoplasm, which resulted in the increase of the cytotoxicity and apoptosis of the tumor cells.[48] Very recently, the interactions between raw HNTs and DOX were confirmed as forming a kind of complex, which is beneficial to high loading capacity and sustained release.[49]

Although the CS-grafted HNTs have an improvement of anticancer drug delivery and apoptosis of the tumor cells,[28] the grafted CS layer on the HNTs surface leads to a significant shielding effect of the nanotube due to the high molecular weight of CS. The surfaces of HNTs were shielded by covalent modification of CS, which leads to decreased surface areas, declined drug-loading ability, and weakened cell uptake ability. In the present work, we proposed chitosan oligosaccharide (with relatively low molecular weight)-modified HNTs to enhance the tumor-targeted delivery of DOX and improve its antitumor efficacy by a dual targeted strategy of mitochondria and nuclei. Chitosan oligosaccharide-grafted HNTs (HNTs-*g*-COS) showed significantly improvement of cytocompatibility and decrease of hemolysis ratio in comparison to unmodified HNTs. DOX-loaded HNTs-*g*-COS (DOX@HNTs-*g*-COS) was prepared via physical absorption process. The cellular uptake of DOX@HNTs-*g*-COS was confirmed by fluorescence microscope and flow cytometry. As displayed in Scheme 1, we hypothesized that HNTs-*g*-COS would promote the anticancer efficiency of DOX through synergistic mechanism of both the mitochondria and nuclei injury. The drug-loaded nanotubes can penetrate the plasma membrane directly and/or via endocytosis mechanism due to their unique needle-like morphology similar to that of carbon nanotubes.[50]

To further evaluate antitumor ability of the DOX@HNTs-*g*-COS in vivo, an animal model of 4T1-bearing mice was established, and the mice were administrated with DOX@HNTs-g-COS through orthotopic injection. DOX@HNTs-*g*-COS treatment group displayed distinctly therapeutic effect and the mice showed the longest survival time up to 60 days. Hematoxylin and eosin (HE) histology of tumors was also performed to evaluate the antitumor efficacy and the toxicity toward different tissues. Overall, the prepared HNTs-*g*-COS have promising applications as anticancer drug delivery and the DOX@HNTs-*g*-COS will provide new opportunities for tumor treatment in clinical applications by both mitochondrial injury pathway and nuclei damage pathway.

2. EXPERIMENTAL SECTION

2.1. Materials. Halloysite nanotubes (HNTs) were purchased from Guangzhou Runwo Materials Technology Co., Ltd. (China). Before experiments were conducted, HNTs were purified to remove the impurity.[51] Chitosan oligosaccharide (COS) was purchased from Dalian GlycoBio Co., Ltd. (China). Doxorubicin hydrochloride (DOX) was purchased from Nanjing Oddfoni Biological Technology

DOI: 10.1021/acsami.6b09074
ACS Appl. Mater. Interfaces 2016, 8, 26578−26590

Co. Ltd. (China). Ultrapure water was produced from Milli-Q water system. 3-Aminopropyltriethoxysilane (APTES), tetrahydro-2,5-dioxofuran, *N*-(3-(dimethylamino)propyl)-*N*′-ethylcarbodiimide (EDC), and *N*-hydroxysuccinimide (NHS) were purchased from Aladdin. Fluorescein isothiocyanate isomer I (FITC) was purchased from Nanjing Keygen Biotech Co., Ltd. and 4′,6-diamidino-2-phenylindole (DAPI) was purchased from Guangzhou Jetway Biotech Co., Ltd. All other chemicals were used as purchased (Aladdin) without further purification.

2.2. Synthesis of COS-Grafted HNTs. COS-grafted HNTs (HNTs-*g*-COS) were synthesized according to previous study with slight modification.[25,28] Scheme 1A shows the synthesis procedure for HNTs-*g*-COS. A certain amount of acetic acid was dropped into 100 mL of 95% ethyl alcohol aqueous solution to adjust pH to 4, and then 20 g of KH-550 was added into the mixture under stirring at 40 °C. Afterward, 5 g of HNTs were added into the solution by stirring for 15 min and ultrasonically treated for another 30 min to obtain good dispersion state of HNTs. After reaction for 24 h, the product of amide groups-grafted HNTs (HNTs-NH_2) were washed by anhydrous ethanol to remove ungrafted KH-550 and completely dried at 50 °C in vacuum oven. The 2 g of HNTs-NH_2 and 1 g of succinic anhydride were reacted in 80 mL of *N*,*N*-dimethylformamide (DMF) by stirring and ultrasonic treatment at 25 °C for 1 day. HNTs-COOH were obtained by washing the product with ultrapure water. HNTs-COOH (2 g) and EDC (1.5 g) were then dispersed in 150 mL of ultrapure water for 10 min. Then 1 g of NHS and 0.5 g of COS were added into the solution in sequence. After being stirred for 12 h, HNTs-*g*-COS were obtained by centrifugation, washing three times with water, and drying at 40 °C in vacuum.

2.3. Characterization of HNTs-*g*-COS. HNTs-*g*-COS were characterized by transmission electron microscopy (TEM), ζ-potential, dynamic light scattering (DLS), Fourier transform infrared spectroscopy (FTIR), thermogravimetric analysis (TGA), X-ray photoelectron spectroscopy (XPS), water contact angle (WCA), and Barrett−Joyner−Halenda (BJH). For TEM observation, HNTs-*g*-COS aqueous solution (the concentration was 0.05%) was dispersed onto holey carbon film on copper grids and observed using a Philips Tecnai 10 TEM machine under an accelerating voltage of 100 kV. The DLS analysis and ζ-potential were measured on a Nano-ZS instrument (Malvern Instruments Limited). FTIR was analyzed by Bruker FTIR from 4000 to 400 cm^{-1}. TGA was carried out by Mettler-Toledo TGA/DSC3+. The temperature was controlled from room temperature to 700 °C at a heating rate of 10 °C/min under a N_2 atmosphere. The percentage of grafting of HNTs was calculated using the following equation: grafting ratio (%) = $(m_1/m_2) \times 100\%$, where m_1 (g) is the weight of organics grafted onto HNTs and m_2 (g) is the weight of HNTs. XPS was carried out by USA Thermo (ESCALAB250Xi). The atomic percent can be calculated. WCA was measured with KRUSS drop shape analyzer DSA 100 instrument at 25.0 ± 0.1 °C. Before determination, the four different HNTs were pelleted by a universal tablet compression machine. The water droplet volume was 11.0 ± 0.5 μL. BJH pore analysis was analyzed by automated surface area and pore size analyzer (TriStar II 3020, Micromeritics Instrument Corporation, Norcross, GA, USA), respectively.

2.4. Drug-Loading Studies. The DOX was dissolved in ultrapure water (50 μg mL^{-1}), and then 100 mg of HNTs-*g*-COS was added into 100 mL of DOX solution. After the solution was stirred for 24 h, the DOX-loaded HNTs-*g*-COS (DOX@HNTs-*g*-COS) was obtained by centrifugation at 4000 rpm for 10 min and washing twice with ultrapure water.[52] The supernatant liquid was collected to measure the absorbance. The adsorption of DOX was calculated using an ultraviolet spectrophotometer at 480 nm. For comparison, raw HNTs were also loaded DOX with a similar procedure, and the DOX-loaded HNTs were denoted as DOX@HNTs. The standard curve of DOX in ultrapure water was given in Figure S1 of the Supporting Information.

$$\text{entrapment efficiency (\%)} = \frac{\text{total amount of DOX} - \text{free DOX}}{\text{total amount of DOX}} \times 100\%$$

$$\text{loading efficiency (\%)} = \frac{\text{weight of loaded DOX}}{\text{total weight of nanoparticles and loaded DOX}} \times 100\%$$

To investigate the interactions between DOX and HNTs-*g*-COS, the ultraviolet visible (UV/vis) absorption spectrum and fluorescence spectra of DOX, HNTs-*g*-COS, and DOX@HNTs-*g*-COS were measured. The excitation wavelength of DOX was set at 480 nm.

2.5. Release Behavior of DOX from DOX@HNTs-*g*-COS. Twenty milligrams of DOX@HNTs-*g*-COS was added into 2 mL of PBS and 2 mL of glioma cell lysate with constant shaking at 37 °C in an Eppendorf tube. At specific times during incubation, the solution was centrifuged at 10 000 rpm for 2 min, then the 1.5 mL of supernatant liquid was taken away to measure the released DOX from DOX@HNTs-*g*-COS via ultraviolet spectrophotometer, and the same volume of fresh PBS and cell lysate were supplied in the release medium.

2.6. Hemocompatibility of HNTs-*g*-COS. Five milliliters of fresh rabbit blood was added into 10 mL of PBS solution and then centrifuged at 1000 rpm for 10 min. After that, the supernatant liquid was thrown. This procedure was repeated three times and the red blood cells (RBCs) were collected. Then 320 μL of RBCs were added into 1680 μL of PBS solution. Twenty-five microliters of RBCs suspension was further added into 500 μL of raw HNTs and HNTs-*g*-COS PBS solution (1 mg mL^{-1}). After being vibrated slightly, the RBCs suspension was incubated at 37 °C for 2 h. After incubation, all the samples were centrifuged at 1000 g at 4 °C. One hundred fifty microliters of the supernatant liquid was transferred into a 96-well plate. The hemolysis ratio was determined by measuring the absorbance at 570 nm using a microplate reader.[28] The positive control group was 100% hemolysis (in ultrapure water) and the negative control group was 0% hemolysis (in PBS solution). The hemolysis ratio was calculated using the following equation:

$$\text{hemolysis ratio(\%)} = \frac{\text{sample absorbance} - \text{negative control}}{\text{positive control} - \text{negative control}} \times 100\%$$

2.7. Cells and Cell Culture Conditions. Human breast cancer cells (MCF-7) and human normal liver cells (L02) were cultured in DMEM supplemented with 10% FBS and 1% penicillin/streptomycin in a humidified atmosphere containing 5% CO_2. The murine breast cancer (4T1) cells were purchased from the Cell Bank of the Chinese Academy of Sciences (Shanghai, China). 4T1 cells were grown in DMEM medium supplemented with 10% fetal bovine serum at 37 °C in a humidified atmosphere containing 5% CO_2.

2.8. MTT Assay. MCF-7 and L02 cells (1×10^4 cells per well) were seeded in 96-well tissue culture plates for 24 h and then incubated with the HNTs-*g*-COS, DOX, and DOX@HNTs-*g*-COS at different concentrations (0, 1, 2, 5, 10, and 20 μg mL^{-1}) for 24 h. It should be noted that the concentration of HNTs-*g*-COS was equal to DOX@HNTs-*g*-COS. After incubation for 24 h, 20 μL/well of MTT solution (5 mg mL^{-1} in PBS) was added into each well. After 4 h, the culture medium was removed and replaced with 150 μL/well of DMSO. To remove the influence of HNTs-*g*-COS and DOX@HNTs-*g*-COS precipitation, 100 μL of supernatant liquid was removed to new 96-well tissue culture plates. The DMSO solution was measured at 570 nm by a microplate reader.

To visualize the MCF-7 cells after treatment with different drugs. MCF cells (1×10^4 cells per well) were seeded in 96-well tissue culture plates for 24 h, HNTs, HNTs-*g*-COS, DOX, and DOX@HNTs-*g*-COS were added to make DOX-equivalent 10 μg mL^{-1}. After incubation for 24 h, cells were stained with 10 μL mixtures of acridine orange (AO, 100 μg mL^{-1}) and ethidium bromide (EB, 100 μg mL^{-1}),

DOI: 10.1021/acsami.6b09074
ACS Appl. Mater. Interfaces 2016, 8, 26578−26590

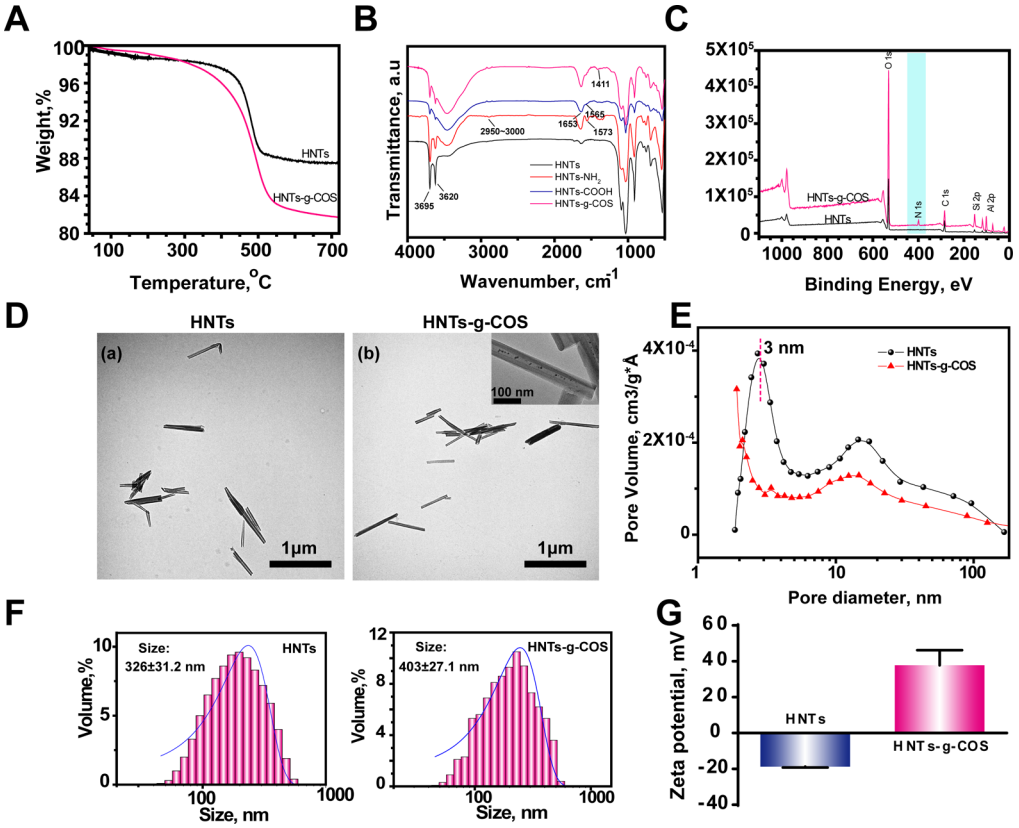

Figure 1. TGA (A), FT-IR spectra (B), XPS spectra (C), TEM (D), BJH pore analysis (E), DLS result (F), and ζ-potentials (G) of HNTs-*g*-COS.

and the cells were immediately examined under a fluorescent microscope (EVOS FL Cell Imaging System).

2.9. Cellular Uptake of DOX@HNTs-*g*-COS. MCF-7 cells were seeded in a six-well plate at a density of 1×10^5 cells per well and cultured in DMEM medium for 24 h. Then the cells were treated with a series of equivalent concentrations of DOX, DOX@HNTs, and DOX@HNTs-*g*-COS (DOX equivalent concentration 20 μg mL^{-1}) for 4 h. The culture media were discarded, and MCF-7 cells were washed three times with cool PBS. Then the MCF-7 cells were treated with enzymes and collected in cool PBS. Then the DOX fluorescence intensity was analyzed by flow cytometer (FACS Gallios, Beckman, USA). The process of entering cells of DOX@HNTs-*g*-COS can be traced by the red fluorescence of DOX. MCF-7 cells (2×10^4 cells) were cultured in Petri dishes in DMEM culture media at 37 °C for 24 h. The culture media was discarded and then 1 mL of fresh DMEM culture media containing DOX or DOX@HNTs-*g*-COS (equivalent concentration of DOX 40 μg mL^{-1}) were added into the well. The process of entering cells of DOX and DOX@HNTs-*g*-COS were captured by EVOS FL Cell Imaging System and laser scanning confocal microscope (CLSM, 510Meta Duo Scan; Carl Zeiss, Germany) at the designed time. Before observation, the MCF-7 cells were counterstained with FITC and DAPI.

2.10. Cell Apoptosis Assay. MCF-7 cells were seeded in six-well plates (5×10^5 cells per well), then the cell culture medium was discarded, and 1 mL of fresh cell culture medium and containing HNTs-*g*-COS, DOX, and DOX@HNTs-*g*-COS (equivalent concentration of DOX was 20 μg mL^{-1}) were added. MCF-7 cells then were trypsinized, centrifuged, washed with PBS, and stained with Annexin V and propidium iodide (PI) following the operating instructions. Both PI and the intracellular DOX exhibited red fluorescence. However, the light intensity and the amount of PI were much higher than those of intracellular DOX. So, the red fluorescence of DOX had little effect on the apoptosis results. MCF-7 cells were quantified using flow cytometry (FACS Gallios, Beckman, USA).

2.11. Measurement and Imaging of Reactive Oxygen Species (ROS). MCF-7 cells were cultured with DMEM media in 24-well plate at a density of 1×10^5 cells per well. Then the culture media was discarded, and 1 mL of fresh DMEM culture media containing DOX or DOX@HNTs-*g*-COS (equivalent concentration of DOX was 20 μg mL^{-1}) was added at 1, 2, 4, 8, 12, and 24 h, respectively. At the designed time, the dihydrorhodamine 123 was added into the cell culture media. After incubation for 30 min, the ROS green fluorescence was shot by EVOS FL Cell Imaging System.

To investigate the drug concentration and time on the ROS production, MCF-7 cells and L02 cells were cultured with DMEM media in a 96-well plate at a density of 1×10^5 cells per well. Then the culture media was discarded, and 100 μL of fresh DMEM culture media and 100 μL of DOX or DOX@HNTs-*g*-COS with equivalent concentration of DOX 1, 2.5, 5, 10, and 20 μg mL^{-1} was added for 12 h, respectively. One hundred microliters of fresh DMEM culture media and 100 μL of DOX or DOX@HNTs-*g*-COS with concentration equivalent of DOX 10 μg mL^{-1} was added into MCF-7 cells for 1, 2, 4, 8, 12, and 24 h, respectively. Then dihydrorhodamine 123 was added into the cell culture media. After incubation for 30 min, the culture media were washed with PBS twice. Finally, the fluorescence intensity was detected by fluorescence microplate (Spectra Max M5, Bio-Tek) at 507 nm.

2.12. Mitochondria Breakage Study. MCF-7 cells (5×10^4 cells) were cultured in Cells Petri dishes in DMEM culture media at 37 °C for 24 h and then DOX or DOX@HNTs-*g*-COS was added. At the specific time, Rhodamine 123 was added into the cell culture. The morphology of the MCF-7 cells was observed by a EVOS FL Cell Imaging System.

2.13. Animals Models. Seven-week-old female BALB/c mice weighing 18−22 g were purchased from Guangdong Medical Laboratory Animal Center (Guangzhou, China), with permission No. SCXK 2011-0015. All mice were kept in a specific pathogen-free animal room at the temperature (23 ± 1 °C) with a 12 h dark-light cycle and fed with standard laboratory diet and water. The animals were allowed to acclimatize to the environment for a week before the experiment. All animal care and experimental procedures were approved by the Animal Care and Use Committee of Jinan University

DOI: 10.1021/acsami.6b09074
ACS Appl. Mater. Interfaces 2016, 8, 26578−26590

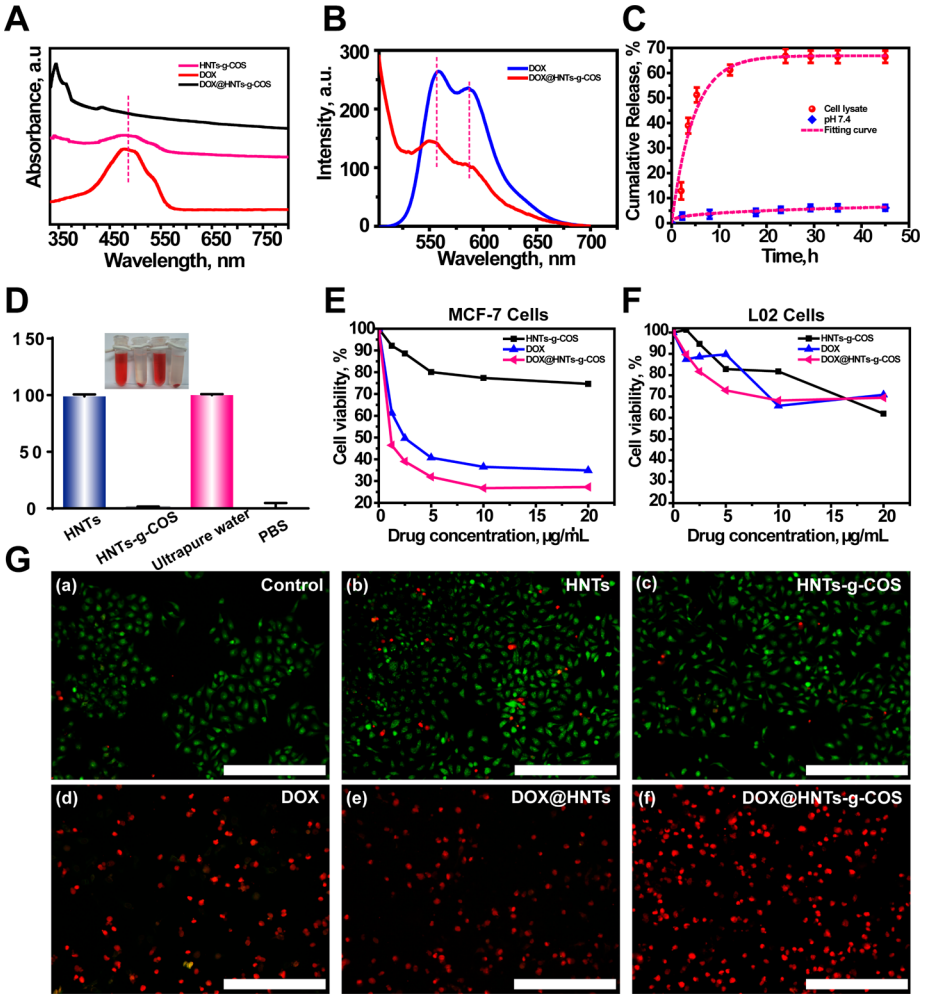

Figure 2. UV/vis absorption spectrum (A) and fluorescence wavelength (B) of HNTs-*g*-COS, DOX, and DOX@HNTs-*g*-COS. The release curves of DOX@HNTs-*g*-COS in PBS and cell lysate (C). The hemolysis ratio of HNTs and HNTs-*g*-COS (D). Cell viability of HNTs-*g*-COS, DOX, and DOX@HNTs-*g*-COS toward MCF-7 cells (E) and L02 cells (F) at different concentrations. The AO-EB staining of MCF-7 cells after treatment with control (a), HNTs (b), HNTs-*g*-COS (c), DOX (d), DOX@HNTs (e), and DOX@HNTs-*g*-COS (f) (DOX equivalent concentration was 10 μg mL^{-1}) for 24 h (G). Scale bar in (G) is 400 μm.

(Approval ID: 20150310001) and were in accordance with the National Institute of Health's Guide for the Care and Use of Laboratory Animals.

2.14. In Vivo Antitumor Efficacy and Systemic Toxicity. MCF-7 cells could cause tumor formation of nude mice, but the operating was rigorous. So 4T1 (mouse mammary cancer cell line) cell was used to induce the formation of mammary tumors in the following animal experiment. 4T1 cells were injected into the second mammary fat pad of BALB/c mice. When the tumor reached about 5 mm in diameter, the mice were randomly allocated into four groups named "control", "HNTs-*g*-COS", "DOX", and "DOX@HNTs-*g*-COS", respectively. The mice were intratumorally injected twice a week for 2 weeks with 100 μL of saline, HNTs-*g*-COS, DOX (20 mg/kg), or DOX@HNTs-*g*-COS (20 mg/kg DOX), respectively, using a 26-gauge needle and a disposable syringe (1 mL). The body weight of mice was monitored every day. The tumor growth was measured through the two perpendicular tumor diameters with a caliper every 3 days, and the tumor volume was calculated by the following formula: volume (mm^3) = 0.5 × [length (mm)] × [width (mm)]^2. The survival of mice was monitored every day for 60 days. The above animal treatment protocol was repeated, and the mice were sacrificed with diethyl ether after 2 weeks drug injection, and tumors, lungs, livers, kidneys, and hearts were collected, weighted, 4% paraformaldehyde-fixed, paraffin-embedded, and sectioned at a thickness of 4 μm for HE staining. Besides, the sections of tumor tissue were also detected by TdT-mediated dUTP Nick-End Labeling (TUNEL) assay.

3. RESULTS AND DISCUSSION

3.1. Synthesis and Characterization of the HNTs-*g*-COS. HNTs-*g*-COS were synthesized according to our previous study and characterized by TGA, FTIR, WCA, ζ-potential, XPS, BJH, DLS, and TEM. Figure 1A compares the TGA curve of HNTs-*g*-COS and raw HNTs. It can be seen that HNTs-*g*-COS have more weight loss than raw HNTs from 285−700 °C. The weight loss of raw HNTs loss in this temperature range is assigned to hydroxyl group dehydration, while the weight loss of HNTs-*g*-COS is not only attributed to the dehydration but also to the degradation of COS. The grafting ratio is calculated to be 6.66%. Figure 1B shows the FTIR spectra for different HNTs. Raw HNTs show typical absorption peaks around 3695, 3620, 1025, and 910 cm^{-1}, which assigned to O−H stretching peak of inner-surface hydroxyl groups, O−H stretching peak of inner hydroxyl groups, Si−O stretching peak of silica group, and O−H deformation of inner hydroxyl groups, respectively.[53] After grafting APTES, HNTs-NH_2 show the C−H bond stretching of APTES around 3000−2950 cm^{-1}. Also, the 1573 cm^{-1} attributed to the N−H group vibration in plane is

DOI: 10.1021/acsami.6b09074
ACS Appl. Mater. Interfaces 2016, 8, 26578−26590

observed in the spectra of HNTs-NH_2. For HNTs-COOH, carbonyl vibrations peaks are observed at 1565 and 1653 cm^{-1} which is attributed to the amide and carboxylic acid groups, respectively.[25] And 1411 cm^{-1} attributed to $-CH_2$ bending of COS are found in the HNTs-*g*-COS.[54] Figure 1C shows in the XPS analysis of raw HNTs and HNTs-*g*-COS. N 1s peak appears in the HNTs-*g*-COS sample and the peak of O 1s becomes higher than that of raw HNTs. Figure S2 shows the atomic content of HNTs-*g*-COS. The N atomic content is determined as 3.63%. So, from the TGA, FTIR, and XPS analysis, COS is successfully grafted on HNTs. Figure S3 shows the WCA of the four HNTs, after modification by APTES, the hydrophobic property of HNTs-NH_2 is increased. Thereafter, the carboxyl groups are grafted on HNTs, and the WCA of HNTs-COOH decreases distinctly due to the hydrophilicity of carboxyl groups. Finally, after reacting with COS, HNTs-*g*-COS show a WCA of 23.9° due to the hydrophilicity of COS.

Figure 1D shows a TEM image of HNTs and HNTs-*g*-COS. HNTs show typical tubular structure with empty lumen. The diameter of HNTs is in the range of 30−50 nm and the length varies in the range of 200−1000 nm. After grafting COS, no obvious morphology changes can be found in the HNTs-*g*-COS; and the lumen structure of HNTs is reserved (inset in (b)). These suggest that the grafting process does not harm the tubular structure. As COS is an oligomer with low molecular weight of ∼3000 Da, one cannot see a layer of polymer around the tube surface. This is different from previously reported polymer-grafted HNTs systems in which a thick layer of polymer layer locates in the HNTs surface.[21,55,56] Figure 1E shows the BJH analysis of HNTs and HNTs-*g*-COS. The peaks around 3, 20, and 50 nm are attributed to surface defects, the lumens of the nanotubes, and pores among the tubes, respectively.[57] After grafting of COS, the peak at 3 nm disappears. Also, the pore volume of HNTs-*g*-COS is less than that of raw HNTs. The pore analysis results support the successful grafting of COS on HNTs surface. Figure 1F indicates the size distribution of HNTs and HNTs-*g*-COS. Both raw HNTs and HNTs-*g*-COS show a relatively narrow size distribution. The average diameter of HNTs-*g*-COS is 403 nm which is 77 nm bigger than that of raw HNTs. The size below 300 nm of HNTs and HNTs-*g*-COS occupy the proportion of 71.0% and 69.4%, respectively. The size and morphology (tubular-like) of HNTs-*g*-COS is necessary for entering cell and drug delivery.[50,58] Figure 1G compares the ζ-potential of raw HNTs and HNTs-*g*-COS. HNTs show a negatively charged surface (−18.73 mV), while HNTs-*g*-COS show a positively charged surface of ζ-potential of +37.77 mV. As is known, the cell membrane is negatively charged; the positive charge of HNTs-*g*-COS can enter cells easier than raw HNTs.

3.2. In Vitro DOX Loading and Releases of HNTs-*g*-COS, the Hemocompatibility, and Cytotoxicity of DOX@HNTs-*g*-COS on MCF-7 Cells and L02 Cells. Figure 2A shows UV/vis absorption spectrum of HNTs-*g*-COS, DOX, and DOX@HNTs-*g*-COS. DOX has the maximum absorption peak at 480 nm, while HNTs-*g*-COS have no peak in this region. After DOX is loaded in HNTs-*g*-COS, the DOX@HNTs-*g*-COS still have the maximum absorption peak at 480 nm, and the peak becomes weak because the DOX is loaded into the surfaces of HNTs-*g*-COS. This phenomenon also reveals that the loading of DOX onto HNTs-*g*-COS is physical absorption process rather than chemical binding, which will not influence the drug activities of DOX.[59] Figure 2B shows the photoluminescence (PL) spectra of DOX@HNTs-*g*-COS and free DOX. The fluorescence spectrum showed that DOX has two fluorescence emission peaks at 555 and 585 nm after excitation with a 480 nm laser. It is also found that the emission peaks location of DOX is not changed. From Figure 2A,B, DOX is loaded onto HNTs-*g*-COS and this loading process does not alter the properties of DOX. Figure S4 shows the appearance of HNTs-*g*-COS, DOX, and DOX@HNTs-*g*-COS in aqueous solution. HNTs-*g*-COS can be stably dispersed in water with a solution color of semitransparent white. DOX solution is jacinth, while the DOX@HNTs-*g*-COS solution is semitransparent jacinth. The drug entrapment efficiency and loading efficiency of HNTs-*g*-COS toward DOX are calculated as 55.5 ± 3.8% and 2.63 ± 0.14%, respectively.

Figure 2C shows release curves of DOX@HNTs-*g*-COS in different media. In PBS (pH 7.4), DOX releases from HNTs-*g*-COS slowly, and the cumulative release ratio is only 6.40% at 45 h. While in cell lysate (tumor slightly acidic environment), the escape speed of DOX from HNTs-*g*-COS is faster. After 12 h, the cumulative releasing ratio is up to 61.9%. The drug release process was fitted by different mathematics models. In PBS, the release kinetics fits the Riger-peppas equation ($\ln Q = a + b \ln t$) with a R^2 of 0.9722. While in cell lysate, the release kinetics fits the first-order release model ($\ln(1 - Q) = a + bt$) with a R^2 of 0.96521.[60] It is suggested that DOX releases little in a normal environment, while it releases much faster and thoroughly in a slightly acidic environment. This result provides the theoretical basis for the following animal injection experiment.

Figure 2D compares the hemolysis ratio of raw HNTs and HNTs-*g*-COS at a concentration of 1 mg mL^{-1}. It can be seen that raw HNTs have 99.0% hemolysis ratio at this concentration. Previous reports also show the hemolysis ratio of HNTs is dose dependence.[61] After grafting of COS, the hemolysis ratio of HNTs-*g*-COS obviously decreased with a value of 0.99%. This result indicates that it is safe for orthotopic injection of HNTs-*g*-COS. Figure 2E,F shows the cell viability of MCF-7 cells and L02 cells treated with different groups. It can be seen that HNTs-*g*-COS have the lower toxicity for MCF-7 cells, while DOX and DOX@HNTs-*g*-COS have a great killing effect on MCF-7 cells. DOX@HNTs-*g*-COS (IC_{50} = 1.17 μg mL^{-1}) have greater toxicity than DOX (IC_{50} = 2.43 μg mL^{-1}), suggesting that loading DOX into HNTs-*g*-COS can enhance the toxicity toward MCF-7 cells. HNTs-*g*-COS, DOX, and DOX@HNTs-*g*-COS do not have the obvious toxicity toward L02 cells. Even when the drug concentration is 20 μg mL^{-1}, the cell viability for every group is higher than 65%. These results reveal that this novel DOX nanovehicle can effectively inhibit the proliferation of cancer cells. The disadvantage of the free DOX is that it has a tendency to spread throughout body and releases rapidly into cells including normal cells and tumor cells. This leads to serious side effects such as cardiotoxicity and noncancer cell cytotoxicity in clinic therapy. The superiority of the nanotubes as the nanocarrier of DOX is that the HNTs can prolong drug residence time in the tumor site due to the protective effect. A decreased drug dose for treating cancer and improved therapeutic effect are expected. It also should be noted that free DOX exerts different toxicity effects on L02 cells (IC_{50} > 20 μg mL^{-1}) and MCF-7 cells (IC_{50} = 2.5 μg mL^{-1}). This is due to the fact that DOX-induced apoptosis occurs through a different signal transduction mechanism in normal cells (H_2O_2-dependent), as compared with that in tumor cells (p53-dependent).[62] Also,

DOI: 10.1021/acsami.6b09074
ACS Appl. Mater. Interfaces 2016, 8, 26578−26590

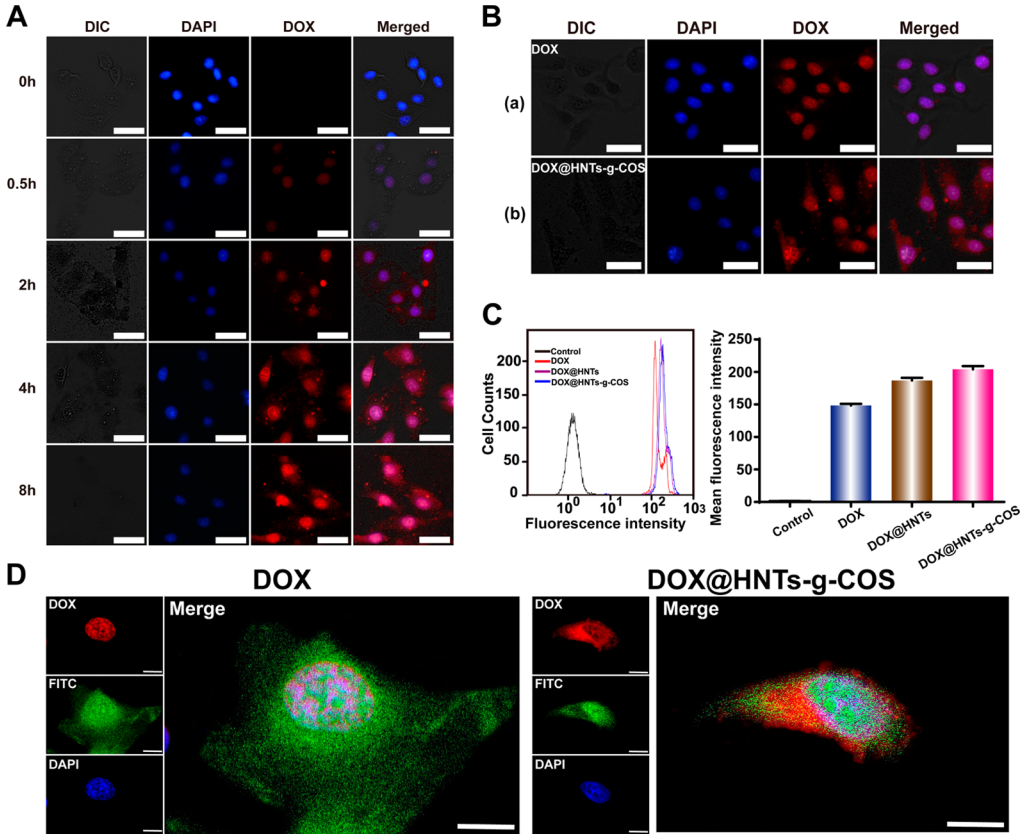

Figure 3. Fluorescence images showing the uptake process of DOX@HNTs-*g*-COS by MCF-7 cells (A). The fluorescence images of MCF-7 cells after treatment with DOX and DOX@HNTs-*g*-COS at 8 h (B). Scale bar is 50 μm. Fluorescence intensity of DOX and quantification fluorescence intensity in MCF-7 cells after treatment with DOX, DOX@HNTs, and DOX@HNTs-*g*-COS (C). CLSM images of cell distribution of free DOX and DOX@HNTs-*g*-COS after incubation for 4 h with MCF-7 cells. Cell cytoskeleton was stained with FITC, and cell nuclei were stained with DOX and DAPI. The final concentration of DOX in the culture medium was 20 μg/mL. Scale bar =10 μm (D).

DOX@HNTs-*g*-COS exhibit a slight inhibition toward human normal cells compared to tumor cells. The killing ability toward tumor cells of DOX@HNTs-*g*-COS will further investigate in vivo.

Figure 2G shows fluorescence images of MCF-7 cells treated by different groups. As is known, AO can enter the living cells which own intact cell membrane, and embed into DNA, making the cell nuclei visualized with a bright green color. EB is unable to enter the live cells, but it can enter the dead cell membrane and the nuclei. Therefore, the dead and late apoptosis cells can be stained a bright red color.[63] It is seen that untreated cells, HNTs-treated cells, and HNTs-*g*-COS-treated cells are bright green, suggesting no apoptosis of MCF-7 cells treated by these materials. However, the cells treated with DOX and DOX@HNTs-*g*-COS (10 μg mL^{-1}) exhibit an intense red fluorescence signal, suggesting a predominant apoptosis after 24 h incubation. The red color of the cell treated with DOX@HNTs-*g*-COS groups is more profound than that of free DOX and DOX@HNTs, suggesting that DOX@HNTs-*g*-COS have the maximum toxicity for MCF-7 cells. This keeps in accordance with the MTT assay above. The optical image of MCF-7 cells after treatment with PBS, HNTs, HNTs-*g*-COS, DOX, and DOX@HNTs-*g*-COS (Figure S5) also indicates the high cytotoxicity of the DOX@HNTs-*g*-COS.

3.3. Uptake of DOX@HNTs-*g*-COS by MCF-7 Cells. From the previous work of Lvov and co-workers, cell uptake of fluorescently labeled HNTs demonstrated the location of HNTs within the cells is in the nuclear vicinity.[20] Figure 3A shows the cellular uptake and intracellular accumulation of DOX@HNTs-*g*-COS for MCF-7 cells. MCF-7 cells treated by DOX@HNTs-*g*-COS with the equivalent drug concentration DOX of 20 μg mL^{-1} were cultured at 37 °C for 0, 0.5, 2, 4, and 8 h. DOX red fluorescence is observed at the first 0.5 h, and the fluorescence intensity increases with the culture time. It is considered that the DOX released from the DOX@HNTs-*g*-COS can be divided into two stages. At the beginning, the weakly bonded DOX will release from the nanocarrier quickly, and they can accumulate in the cell nuclei region and combine the DNA easily. Afterward, the strongly bonded DOX together with the HNTs-*g*-COS transfer the cytomembrane and enter the cytoplasm. So, the red fluorescence of the nuclei can be seen as early as 0.5 h. After 4 h incubation, the red fluorescence appeared in the cytoplasm.

Figure 3B shows the cellular uptake of DOX and DOX@HNTs-*g*-COS at the time of 8 h. In comparison of DOX and DOX@HNTs-*g*-COS, it is found that the red fluorescence of DOX@HNTs-*g*-COS in cells is brighter than that of DOX-treated cells. The free DOX is directly embedded in the cell nuclei with a few in the cell cytoplasm. It is considered that free DOX can rapidly diffuse across both the cell and nuclear membranes.[47] DOX@HNTs-*g*-COS are internalized by the endocytosis mechanism and/or penetration mechanism (similar to a "nanosyringe") and can be retained both in the cell cytoplasm and nuclei with a prolonged residue time. This provides the possibility of another mechanism of inducing cell apoptosis via mitochondrial injury pathway which will be

DOI: 10.1021/acsami.6b09074
ACS Appl. Mater. Interfaces 2016, 8, 26578−26590

shown in the following section. The nanoparticles with a cylindrical shape and a high aspect ratio, such as carbon nanotubes, are considered with the ability to penetrate cytomembrane by energy-independent mechanisms.[50] This different intracellular distribution between DOX group and DOX@HNTs-*g*-COS group in MCF-7 cells is a key factor that influences the killing and apoptosis ability toward tumor cells. DOX@HNTs-*g*-COS retained in the cytoplasm can hurt more mitochondria than free DOX. Overall, these results confirm the fact that HNTs-*g*-COS can enter MCF-7 cells and enhance the efficacy of DOX drug.

Figure 3C shows the quantitative fluorescence intensity of DOX in MCF-7 cells determined by a flow cytometer. On account of the congenital fluorescence of DOX (E_x = 480 nm, E_m = 590 nm), it is convenient to assess the uptake ability of the drug by the cells. Among the four groups, DOX@HNTs-*g*-COS have the strongest fluorescence intensity in cells and is about 1.4 times higher than free DOX. Because of the positively charged surface of HNTs-*g*-COS, it can enter into the cell membrane more easily than raw negatively charged HNTs. So, the DOX@HNTs group has a lower fluorescence intensity compared with the DOX@HNTs-*g*-COS group. The cell uptake results suggest that HNTs-*g*-COS are effective drug nanovehicles which can carry drugs and enter into the cells.

On the basis of the DOX releasing result in Figure 2C, DOX releases from HNTs-*g*-COS slowly, and the cumulative release ratio is 61.9% after 12 h. In contrast, free DOX releases in the same condition is very quick (data not shown). The COS-grafted HNTs allowed a controlled sustained release of the loaded DOX due to the interactions between the nanotubes and the drug. Release of DOX from the lumen is rather slow due to its lower diffusion coefficient, as well as to stronger adsorption to the lumen walls. To observe the distribution of DOX and DOX@HNTs-*g*-COS in MCF-7 cells, CLSM images are shown in Figure 3D. It can be seen that the cells cultured with DOX@HNTs-*g*-COS show stronger intracellular red fluorescent signals both in the cell nuclei and cytoplasm after 4 h incubation. However, the free DOX mainly locates in the cell nuclei. The distribution of DOX in the cell is in accord with the previous studies.[64,65] As a result, DOX@HNTs-*g*-COS can hurt more mitochondria than free DOX which will also be illustrated below.

3.4. Apoptosis Process of MCF-7 Cells Induced by DOX@HNTs-*g*-COS. The effect of HNTs-*g*-COS, DOX, and DOX@HNTs-*g*-COS on apoptosis was investigated by Annexin V and PI double staining and analyzed via flow cytometry (Figure 4). MCF-7 cells treated with HNTs-*g*-COS display no obvious apoptosis phenomenon with total apoptosis ratio of 6.8% (a sum of the early apoptosis ratio of 0.32% and the late apoptosis ratio of 6.48%) as well as a control group. With the cells treated with DOX@HNTs-*g*-COS (drug equivalent concentration is 10 μg mL^{-1}), there is a 64.35% apoptosis ratio which is higher than 51.0% for free DOX-treated group. This again confirms the enhanced anticancer efficacy in vitro via the surface functionalization of HNTs by grafting COS.

ROS overproduction is supposed to reveal an essential chemical signal that reflects the cell apoptosis. Generally, excess intracellular ROS can attack various biological molecules, breaking the redox balance of the cells, leading to DNA damage and cell apoptosis through downstream signaling pathways.[66] Herein, the levels of ROS generation in the MCF-7 cells exposed to DOX@HNTs-*g*-COS and free DOX was

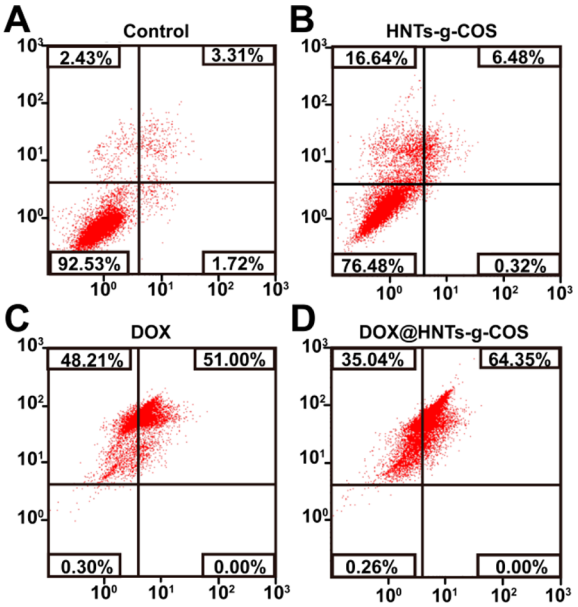

Figure 4. Apoptosis of MCF-7 cells after treatment with PBS (A), HNTs-*g*-COS (B), DOX (C), and DOX@HNTs-*g*-COS (D) (DOX equivalent concentration was 10 μg mL^{-1}) for 24 h.

measured by dihydrorhodamine 123 fluorescence assays. Dihydrorhodamine 123 (without fluoresces itself) is a commonly used ROS probe which can across the membrane via passive diffusion. When the cells are in the apoptosis state by the addition of anticancer drugs, the ROS level rises and reacts with dihydrorhodamine 123. The dihydrorhodamine 123 is oxidized by the ROS and transferred into rhodamine 123, leading to the emergence of the fluorescence. So the fluorescence intensity is related to the amount of ROS. As shown in Figure 5A, for both DOX and DOX@HNTs-*g*-COS group, ROS are generated gradually with the time. After the fluorescence signal is carefully checked, it can be found that the fluorescence of cells treated with DOX@HNTs-*g*-COS group is brighter than that of cells treated with free DOX with the same culture time. This indicates that DOX@HNTs-*g*-COS have a stronger ability for promoting ROS production of cells. As time goes to 24 h, the fluorescence intensity declines, which is because of the clearance of ROS by cells and the death of cells. The fluorescence microscope images and ROS value for the control group without drug treatment are not shown due to the fact that the images are totally black and the ROS amount is nearly zero. The quantitative analysis of ROS level in MCF-7 cells treated by different drugs at different times has been given in Figure S6. The trend is in accord with the fluorescence images shown in Figure 5A. Figure 5B shows the ROS fluorescence intensity caused by different concentrations of DOX and DOX@HNTs-*g*-COS toward MCF-7 cells and L02 cells. The produced ROS increases with the increases of the drug concentration for both groups. Compared with free DOX, DOX@HNTs-*g*-COS can cause more ROS, which is a benefit for the apoptosis of MCF-7 cells. In the normal cells, a similar trend of the ROS generation is observed.

ROS are mainly produced in mitochondria, and the mitochondrial damage easily occurred because of drug attack.[67] Generally, DOX can enter the cell nuclei quickly. Hence, mitochondrial injury pathway induced by free DOX is weak. But the overproduced ROS by drugs can also damage the mitochondria.[68,69] It is considered that the survival state of cells

DOI: 10.1021/acsami.6b09074
ACS Appl. Mater. Interfaces 2016, 8, 26578−26590

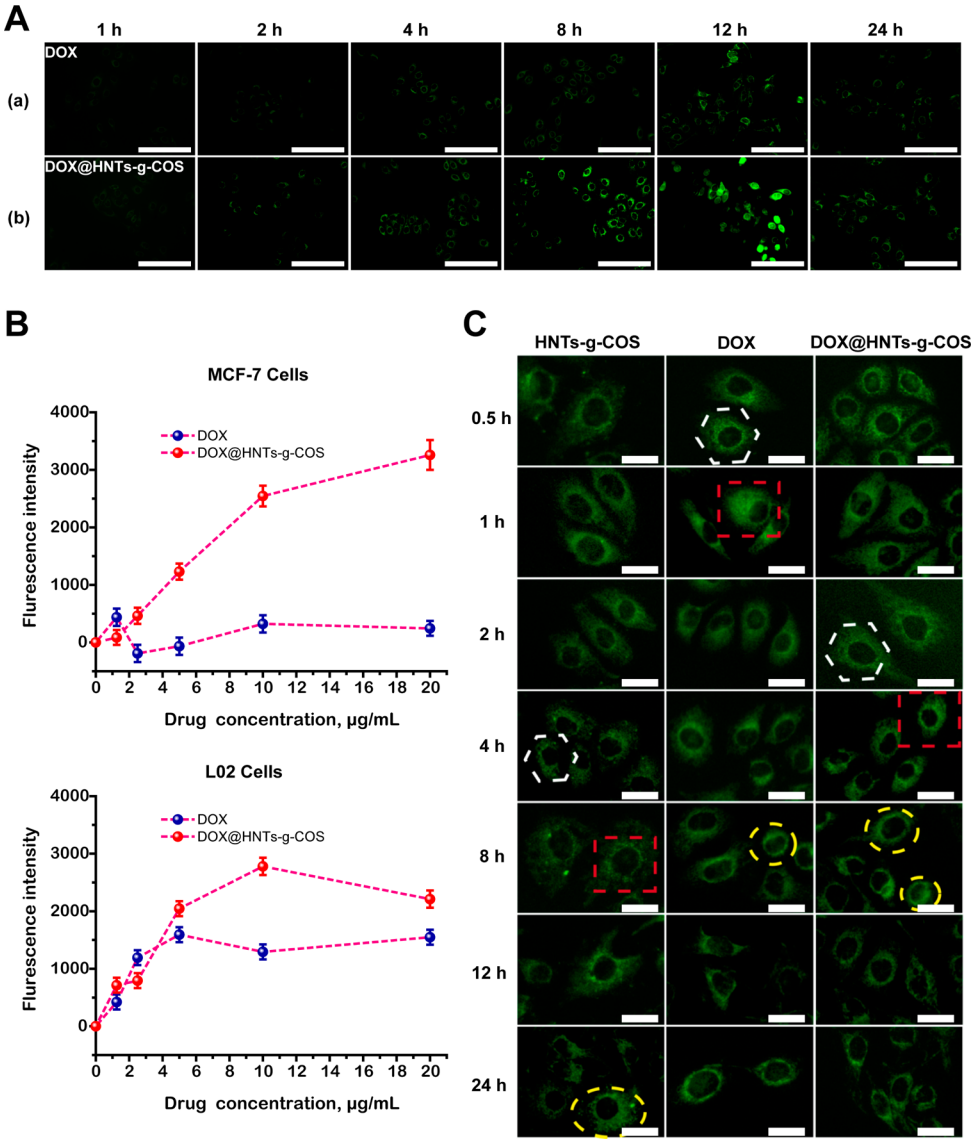

Figure 5. ROS fluorescence image of MCF-7 cells with the time after treatment with DOX and DOX@HNTs-*g*-COS (A) with scale bar of 200 μm. The ROS fluorescence intensity caused by different concentrations of drugs toward MCF-7 cells and L02 cells (B). Mitochondrial morphology observed under EVOS FL Cell Imaging System (C) with scale bar of 50 μm. White hexagon represents mitochondria concentrate, red quadrate represents mitochondria cracks, and yellow oval represents the cytomembrane fracture, mitochondria attached to the nuclei.

depends on the functional status of mitochondria to a great extent.[70] Figure 5C shows the fluorescent photographs which illustrating the changes of mitochondrial morphology. At an early time, the mitochondria are homogeneously dispersed in the cell cytoplasm. The mitochondria concentrate and nonuniformly disperse at 2 h upon treatment with DOX@HNTs-*g*-COS, while this process occurs as early as 0.5 h for the cells treated with free DOX. This is due to the fact that DOX releases more quickly in the free DOX group compared with DOX@HNTs-*g*-COS group in the cellular environment. For the DOX@HNTs-*g*-COS group, the mitochondria crack and concentrate at 4 h. DOX@HNTs-*g*-COS destroys the mitochondria later than DOX, but this does not mean that DOX@HNTs-*g*-COS are not effective, as DOX@HNTs-*g*-COS can be retained in the cytoplasm for a relatively long time. HNTs-*g*-COS can also induce the mitochondria to concentrate and crack but with a relatively long time. The cell membrane begins rupture at 8 h and cytoplasm runs away for the DOX@HNTs-*g*-COS groups. Only the cell nuclei were reserved at 8 h, and mitochondria attach to the nuclei. This phenomenon reveals that DOX@HNTs-*g*-COS can destroy the mitochondria of MCF-7 cells as well as attack the nuclei, in spite of the fact that it occurs later than free DOX.

3.5. In Vivo Antitumor Effects of DOX@HNTs-*g*-COS in 4T1-Bearing Mice. The effects of DOX@HNTs-*g*-COS on antitumor activity of 4T1-bearing mice are shown in Figure 6. Compared with the control group, both the DOX group and DOX@HNTs-*g*-COS group could significantly reduce tumor volume ($P < 0.001$) and tumor weight ($P < 0.05$), while the HNTs-*g*-COS group had no effect on tumor volume. Furthermore, the DOX@HNTs-*g*-COS group could significantly reduce tumor volume ($P < 0.05$) and tumor weight ($P < 0.05$) when compared with the DOX group. The tumor inhibition rate (IR) was 46.13% for the DOX group and 83.47% for the DOX@HNTs-*g*-COS group (Figure 6A,B). Compared with the control group, the body weight of the DOX group was significantly decreased ($P < 0.01$), and the DOX@HNTs-*g*-COS group was also significantly decreased ($P < 0.01$) when

DOI: 10.1021/acsami.6b09074
ACS Appl. Mater. Interfaces 2016, 8, 26578−26590

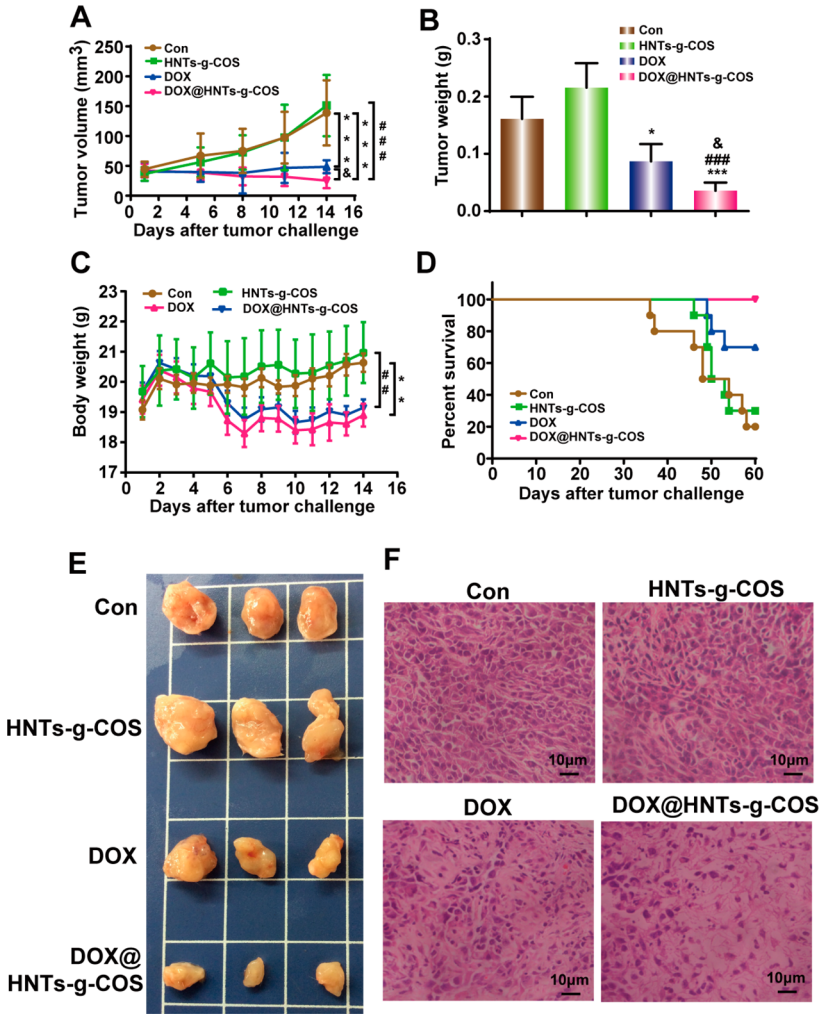

Figure 6. In vivo antitumor effect of DOX@HNTs-*g*-COS in 4T1-bearing mice. Tumor volume changes (A) and tumor weight (B) of 4T1-bearing mice treated with saline, HNTs-*g*-COS, DOX (20 mg/kg), and DOX@HNTs-*g*-COS (20 mg/kg DOX) via intratumoral drug injection. Body weight (C) and Kaplan−Meier curves (D) of tumor-bearing mice in various groups. Excised 4T1 solid tumors (E) and representative micrographs of HE staining (F) of different treatment groups on the 14th day. The values were represented as mean ± SD. The significance of differences from control groups at $^{*}P < 0.05$, $^{**}P < 0.01$, $^{***}P < 0.001$; from HNTs-*g*-COS group at $^{\#\#}P < 0.001$, $^{\#\#\#}P < 0.001$; from DOX group at $^{\&}P < 0.01$.

compared with the HNTs-*g*-COS group. These results indicated that DOX had toxic effects on mice in body weight (Figure 6C). Figure 6D reveals that survival curves of the subcutaneous 4T1-bearing mice in four treatment groups. Eight of 10 mice were dead within 60 days in the control group, and 7 of 10 mice died in the HNTs-*g*-COS group. For the DOX group, 7 mice remained alive after treatment, while all mice treated with DOX@HNTs-*g*-COS survived over 60 days. In comparison, the group that received DOX@HNTs-*g*-COS treatment displays distinctly therapeutic effects. The median survival time for the control group and HNTs-*g*-COS group was 51 and 51.5 days, respectively, while the median survival time for DOX group and DOX@HNTs-*g*-COS group were not reached. These results suggest that DOX@HNTs-*g*-COS could effectively improve the survival ratio of 4T1 tumor-bearing mice. Excised 4T1 solid tumors are shown in Figure 6E. Compared to saline group (negative control), two DOX formulations exhibited significant effects on inhibiting tumor growth after injection. Figure 6F shows the HE staining assay of tumors treated with different groups. The negative control and HNTs-*g*-COS group showed typical pathological characteristics of tumor cells such as large and irregularly shaped nuclei while other DOX formulations showed massive cancer cell remission such as tumor coagulative necrosis, nuclei fragmentation, and intercellular blank. Especially, the tumor of DOX@HNTs-*g*-COS group was predominately damaged with decreased tumor cellularity in viable areas. Collectively, these data indicated that DOX@HNTs-*g*-COS had a remarkable antitumor efficacy in vivo.

3.6. Effect of DOX@HNTs-*g*-COS on Apoptosis in Tumor Tissues and Systemic Toxicity. The apoptosis index was examined by TUNEL assay, and the brown spots (the red arrows) in Figure 7A represented the apoptosis in tumor tissue. Both the DOX@HNTs-*g*-COS group and the free DOX group could induce significant apoptosis in tumor tissue ($P < 0.01$), when compared with the control group. It was noted that the apoptosis index of the DOX@HNTs-*g*-COS group (72%) was higher than that of the DOX group (60%) ($P < 0.05$) (Figure 7B). These data indicated that DOX@HNTs-*g*-COS enhanced the antitumor efficacy by inducing apoptosis in vivo. As shown in Figure 7C, the histology and pathology of hearts, lungs, kidneys, and livers tissues from mice with different treatments were observed by HE staining. Compared with the control group, cardiomyocytes from the DOX group were ruptured,

DOI: 10.1021/acsami.6b09074
ACS Appl. Mater. Interfaces 2016, 8, 26578−26590

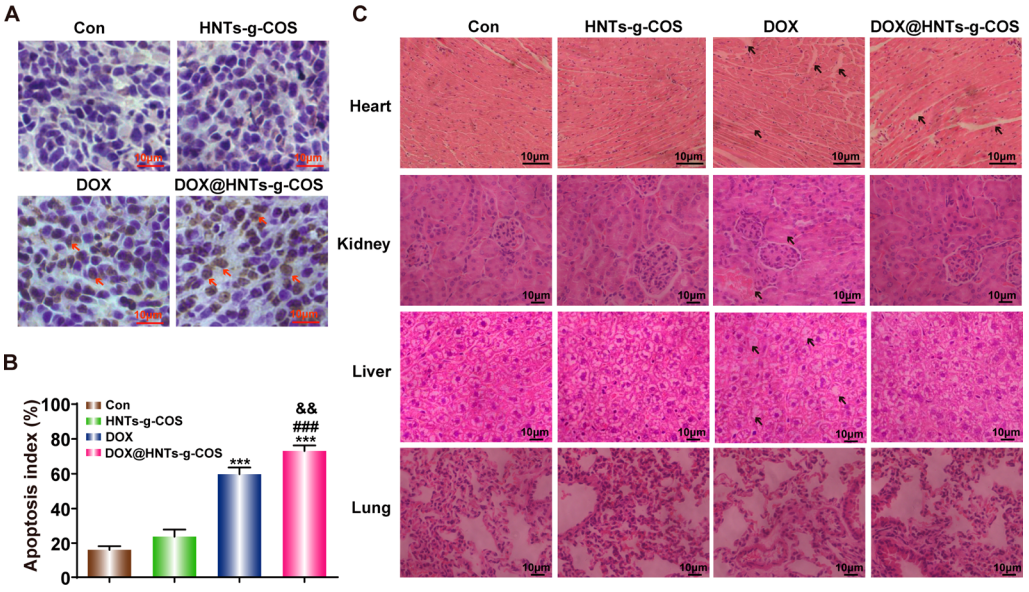

Figure 7. Effects of DOX@HNTs-*g*-COS on apoptosis in tumor tissues and systemic toxicity. Representative photographs of tumor sections examined by TUNEL assay (A). TUNEL-positive cell nuclei (brown spots) were observed. Apoptosis index of different groups (B). The number of apoptosis cells was counted in five random fields in a blinded manner. Histopathology of the major organs in the differently treated 4T1 tumor-bearing mice (C). The arrows in the heart sections indicate certain cardiomyocytes ruptured and scattered; the arrows in kidney sections indicate the deformation necrosis of renal tubes, and the arrows in liver sections indicate the microvesicular steatosis. The values were represented as mean ± SD. The significance of differences from the control group at $^{***}P < 0.001$, from HNTs-*g*-COS group at $^{\#\#\#}P < 0.001$, from DOX group at $^{\&\&}P < 0.01$.

and scattered, while it was less evident in the DOX@HNTs-*g*-COS group. Slight nephrotoxicity and hepatic damage (microvesicular steatosis) were only observed in the DOX group, and lungs showed no distinct toxicity in any treatment group. The degradable behavior in vivo, biodistribution, and excretion from the body of HNTs-*g*-COS are under investigation in our laboratory and will be reported in another paper. All the present results suggest that the DOX@HNTs-*g*-COS are biosafe in vivo.

4. CONCLUSION

In summary, COS-grafted HNTs were synthesized to increase the biocompatibility of HNTs and increase the cellular uptake ability of DOX. TGA, FTIR, XPS, WCA, TEM morphology, DLS, ζ-potential, and BJH pore analysis all support the successful surface functionalization of HNTs by COS. DOX@HNTs-*g*-COS exhibit low hemolysis ratio, favorable biocompatibility, and appropriate drug releasing in vitro. The experiment in vitro demonstrates that DOX@HNTs-*g*-COS can effectively kill MCF-7 cells via promoting apoptosis. DOX@HNTs-*g*-COS can retain both in the cell nuclei and in the cytoplasm, which prompts apoptosis via multiple mechanisms. Compared with free DOX, DOX@HNTs-*g*-COS can cause more ROS production of the tumor cells. DOX@HNTs-*g*-COS can induce mitochondrial injury of MCF-7 cells as well as attack the nuclei. The in vivo antitumor experiments demonstrate that DOX@HNTs-*g*-COS exhibit better efficiency of inhibiting tumor. Also, DOX@HNTs-*g*-COS have fewer ruptured cardiomyocytes compared with free DOX. DOX@HNTs-*g*-COS show no toxicity of hearts, lungs, kidneys, and livers tissues. In total, the rational designed HNTs nanocarrier for chemotherapy drug provides new opportunities for cancer treatment.

■ ASSOCIATED CONTENT

Supporting Information

The Supporting Information is available free of charge on the ACS Publications website at DOI: 10.1021/acsami.6b09074.

The standard curve of DOX at 480 nm; chemical composition of HNTs-*g*-COS; WCA of different HNTs; appearance of HNTs-*g*-COS, DOX, and DOX@HNTs-*g*-COS in aqueous solution; optical image of MCF-7 cells after treatment with PBS, HNTs, HNTs-*g*-COS, DOX, DOX@HNTs, and DOX@HNTs-*g*-COS (equivalent concentration was 20 μg mL^{-1}); ROS fluorescence intensity in MCF-7 cells treated by different drugs at equivalent concentrations of 10 μg mL^{-1} at different times (PDF)

■ AUTHOR INFORMATION

Corresponding Authors

*Tel.: (86)20-85226663. Fax: (86)20-85223271. E-mail: rongronghe@jnu.edu.cn (R.-R.H.).
*E-mail: liumx@jnu.edu.cn (M.L.).

Author Contributions

#The authors contributed equally to this work.

Notes

The authors declare no competing financial interest.

■ ACKNOWLEDGMENTS

This work was financially supported by National High Technology Research and Development Program of China (2015AA020915), the National Natural Science Foundation of China (grant No. 51473069, 81473115, and 51502113), and the Guangdong Natural Science Funds for Distinguished Young Scholar (grant No. S2013050014606 and S20120011316), Science and Technology Program of Guangzhou, China (No. 2013J4100100 and 201610010026), Guang-

DOI: 10.1021/acsami.6b09074
ACS Appl. Mater. Interfaces 2016, 8, 26578−26590

dong Special support program (2014TQ01C127), and the Fundamental Research Funds for the Central Universities (21615204).

REFERENCES

(1) Schroeder, A.; Heller, D. A.; Winslow, M. M.; Dahlman, J. E.; Pratt, G. W.; Langer, R.; Jacks, T.; Anderson, D. G. Treating Metastatic Cancer with Nanotechnology. *Nat. Rev. Cancer* **2012**, *12*, 39−50.

(2) Ferrari, M. Cancer Nanotechnology: Opportunities and Challenges. *Nat. Rev. Cancer* **2005**, *5*, 161−171.

(3) Eetezadi, S.; Ekdawi, S. N.; Allen, C. The Challenges Facing Block Copolymer Micelles for Cancer Therapy: In Vivo Barriers and Clinical Translation. *Adv. Drug Delivery Rev.* **2015**, *91*, 7−22.

(4) Liang, X.; Gao, J.; Jiang, L.; Luo, J.; Jing, L.; Li, X.; Jin, Y.; Dai, Z. Nanohybrid Liposomal Cerasomes with Good Physiological Stability and Rapid Temperature Responsiveness for High Intensity Focused Ultrasound Triggered Local Chemotherapy of Cancer. *ACS Nano* **2015**, *9*, 1280−1293.

(5) Czapar, A. E.; Zheng, Y.-R.; Riddell, I. A.; Shukla, S.; Awuah, S. G.; Lippard, S. J.; Steinmetz, N. F. Tobacco Mosaic Virus Delivery of Phenanthriplatin for Cancer Therapy. *ACS Nano* **2016**, *10*, 4119−4126.

(6) He, L.; Lai, H.; Chen, T. Dual-Function Nanosystem for Synergetic Cancer Chemo-/Radiotherapy through ROS-Mediated Signaling Pathways. *Biomaterials* **2015**, *51*, 30−42.

(7) Orecchioni, M.; Cabizza, R.; Bianco, A.; Delogu, L. G. Graphene as Cancer Theranostic Tool: Progress and Future Challenges. *Theranostics* **2015**, *5*, 710.

(8) Li, J.; Lyv, Z.; Li, Y.; Liu, H.; Wang, J.; Zhan, W.; Chen, H.; Chen, H.; Li, X. A Theranostic Prodrug Delivery System Based on Pt (IV) Conjugated Nano-Graphene Oxide with Synergistic Effect to Enhance the Therapeutic Efficacy of Pt Drug. *Biomaterials* **2015**, *51*, 12−21.

(9) Meng, H.; Wang, M.; Liu, H.; Liu, X.; Situ, A.; Wu, B.; Ji, Z.; Chang, C. H.; Nel, A. E. Use of a Lipid-Coated Mesoporous Silica Nanoparticle Platform for Synergistic Gemcitabine and Paclitaxel Delivery to Human Pancreatic Cancer in Mice. *ACS Nano* **2015**, *9*, 3540−3557.

(10) de la Torre, C.; Casanova, I.; Acosta, G.; Coll, C.; Moreno, M. J.; Albericio, F.; Aznar, E.; Mangues, R.; Royo, M.; Sancenón, F.; Martinez-Manez, R. Gated Mesoporous Silica Nanoparticles Using a Double-Role Circular Peptide for the Controlled and Target-Preferential Release of Doxorubicin in CXCR4-Expresing Lymphoma Cells. *Adv. Funct. Mater.* **2015**, *25*, 687−695.

(11) Yuan, Y.; Ding, Z.; Qian, J.; Zhang, J.; Xu, J.; Dong, X.; Han, T.; Ge, S.; Luo, Y.; Wang, Y.; Zhong, K.; Liang, G. Casp3/7-Instructed Intracellular Aggregation of Fe_3O_4 Nanoparticles Enhances T2MR Imaging of Tumor Apoptosis. *Nano Lett.* **2016**, *16*, 2686−2691.

(12) Goldberg, M.; Langer, R.; Jia, X. Nanostructured Materials for Applications in Drug Delivery and Tissue Engineering. *J. Biomater. Sci., Polym. Ed.* **2007**, *18*, 241−268.

(13) Peer, D.; Karp, J. M.; Hong, S.; Farokhzad, O. C.; Margalit, R.; Langer, R. Nanocarriers as an Emerging Platform for Cancer Therapy. *Nat. Nanotechnol.* **2007**, *2*, 751−760.

(14) Allen, T. M.; Cullis, P. R. Drug Delivery Systems: Entering the Mainstream. *Science* **2004**, *303*, 1818−1822.

(15) Joussein, E.; Petit, S.; Churchman, J.; Theng, B.; Righi, D.; Delvaux, B. Halloysite Clay Minerals - a Review. *Clay Miner.* **2005**, *40*, 383−426.

(16) Lvov, Y. M.; Shchukin, D. G.; Mohwald, H.; Price, R. R. Halloysite Clay Nanotubes for Controlled Release of Protective Agents. *ACS Nano* **2008**, *2*, 814−820.

(17) Liu, M.; Jia, Z.; Jia, D.; Zhou, C. Recent Advance in Research on Halloysite Nanotubes-Polymer Nanocomposite. *Prog. Polym. Sci.* **2014**, *39*, 1498−1525.

(18) Zhao, M.; Liu, P. Adsorption Behavior of Methylene Blue on Halloysite Nanotubes. *Microporous Mesoporous Mater.* **2008**, *112*, 419−424.

(19) Jinhua, W.; Xiang, Z.; Bing, Z.; Yafei, Z.; Rui, Z.; Jindun, L.; Rongfeng, C. Rapid Adsorption of Cr (VI) on Modified Halloysite Nanotubes. *Desalination* **2010**, *259*, 22−28.

(20) Vergaro, V.; Abdullayev, E.; Lvov, Y. M.; Zeitoun, A.; Cingolani, R.; Rinaldi, R.; Leporatti, S. Cytocompatibility and Uptake of Halloysite Clay Nanotubes. *Biomacromolecules* **2010**, *11*, 820−826.

(21) Liu, M.; Wu, C.; Jiao, Y.; Xiong, S.; Zhou, C. Chitosan−Halloysite Nanotubes Nanocomposite Scaffolds for Tissue Engineering. *J. Mater. Chem. B* **2013**, *1*, 2078−2089.

(22) Liu, M.; Zhang, Y.; Wu, C.; Xiong, S.; Zhou, C. Chitosan/Halloysite Nanotubes Bionanocomposites: Structure, Mechanical Properties and Biocompatibility. *Int. J. Biol. Macromol.* **2012**, *51*, 566−575.

(23) Kryuchkova, M.; Danilushkina, A. A.; Lvov, Y. M.; Fakhrullin, R. F. Evaluation of Toxicity of Nanoclays and Graphene Oxide in Vivo: A Paramecium Caudatum Study. *Environ. Sci.: Nano* **2016**, *3*, 442−452.

(24) Frost, R. L.; Kristof, J. Intercalation of Halloysite: A Raman Spectroscopic Study. *Clays Clay Miner.* **1997**, *45*, 551−563.

(25) Joo, Y.; Jeon, Y.; Lee, S. U.; Sim, J. H.; Ryu, J.; Lee, S.; Lee, H.; Sohn, D. Aggregation and Stabilization of Carboxylic Acid Functionalized Halloysite Nanotubes (HNT-COOH). *J. Phys. Chem. C* **2012**, *116*, 18230−18235.

(26) Lee, Y.; Jung, G.-E.; Cho, S. J.; Geckeler, K. E.; Fuchs, H. Cellular Interactions of Doxorubicin-Loaded DNA-Modified Halloysite Nanotubes. *Nanoscale* **2013**, *5*, 8577−8585.

(27) Riela, S.; Massaro, M.; Colletti, C. G.; Bommarito, A.; Giordano, C.; Milioto, S.; Noto, R.; Poma, P.; Lazzara, G. Development and Characterization of Co-Loaded Curcumin/Triazole-Halloysite Systems and Evaluation of Their Potential Anticancer Activity. *Int. J. Pharm.* **2014**, *475*, 613−623.

(28) Liu, M.; Chang, Y.; Yang, J.; You, Y.; He, R.; Chen, T.; Zhou, C. Functionalized Halloysite Nanotube by Chitosan Grafting for Drug Delivery of Curcumin to Achieve Enhanced Anticancer Efficacy. *J. Mater. Chem. B* **2016**, *4*, 2253−2263.

(29) Zhai, R.; Zhang, B.; Liu, L.; Xie, Y.; Zhang, H.; Liu, J. Immobilization of Enzyme Biocatalyst on Natural Halloysite Nanotubes. *Catal. Commun.* **2010**, *12*, 259−263.

(30) Abdullayev, E.; Lvov, Y. Clay Nanotubes for Corrosion Inhibitor Encapsulation: Release Control with End Stoppers. *J. Mater. Chem.* **2010**, *20*, 6681−6687.

(31) Veerabadran, N. G.; Mongayt, D.; Torchilin, V.; Price, R. R.; Lvov, Y. M. Organized Shells on Clay Nanotubes for Controlled Release of Macromolecules. *Macromol. Rapid Commun.* **2009**, *30*, 99−103.

(32) Fu, Y.; Zhao, D.; Yao, P.; Wang, W.; Zhang, L.; Lvov, Y. Highly Aging-Resistant Elastomers Doped with Antioxidant-Loaded Clay Nanotubes. *ACS Appl. Mater. Interfaces* **2015**, *7*, 8156−8165.

(33) Abdullayev, E.; Lvov, Y. Halloysite Clay Nanotubes as a Ceramic "Skeleton" for Functional Biopolymer Composites with Sustained Drug Release. *J. Mater. Chem. B* **2013**, *1*, 2894−2903.

(34) Jing, H.; Higaki, Y.; Ma, W.; Wu, H.; Yah, W. O.; Otsuka, H.; Lvov, Y. M.; Takahara, A. Internally Modified Halloysite Nanotubes as Inorganic Nanocontainers for a Flame Retardant. *Chem. Lett.* **2013**, *42*, 121−123.

(35) Abdullayev, E.; Price, R.; Shchukin, D.; Lvov, Y. Halloysite Tubes as Nanocontainers for Anticorrosion Coating with Benzotriazole. *ACS Appl. Mater. Interfaces* **2009**, *1*, 1437−1443.

(36) Yuan, P.; Southon, P. D.; Liu, Z.; Kepert, C. J. Organosilane Functionalization of Halloysite Nanotubes for Enhanced Loading and Controlled Release. *Nanotechnology* **2012**, *23*, 375705.

(37) Qi, R.; Guo, R.; Shen, M.; Cao, X.; Zhang, L.; Xu, J.; Yu, J.; Shi, X. Electrospun Poly (Lactic-Co-Glycolic Acid)/Halloysite Nanotube Composite Nanofibers for Drug Encapsulation and Sustained Release. *J. Mater. Chem.* **2010**, *20*, 10622−10629.

(38) Shi, Y.-F.; Tian, Z.; Zhang, Y.; Shen, H.-B.; Jia, N.-Q. Functionalized Halloysite Nanotube-Based Carrier for Intracellular Delivery of Antisense Oligonucleotides. *Nanoscale Res. Lett.* **2011**, *6*, 608.

DOI: 10.1021/acsami.6b09074
ACS Appl. Mater. Interfaces 2016, 8, 26578−26590

(39) Gautier, J.; Allard-Vannier, E.; Munnier, E.; Soucé, M.; Chourpa, I. Recent Advances in Theranostic Nanocarriers of Doxorubicin Based on Iron Oxide and Gold Nanoparticles. *J. Controlled Release* **2013**, *169*, 48−61.
(40) Wang, Y.; Zhang, X.; Yu, P.; Li, C. Glycopolymer Micelles with Reducible Ionic Cores for Hepatocytes-Targeting Delivery of DOX. *Int. J. Pharm.* **2013**, *441*, 170−180.
(41) Tacar, O.; Sriamornsak, P.; Dass, C. R. Doxorubicin: An Update on Anticancer Molecular Action, Toxicity and Novel Drug Delivery Systems. *J. Pharm. Pharmacol.* **2013**, *65*, 157−170.
(42) Huan, M.; Zhang, B.; Teng, Z.; Cui, H.; Wang, J.; Liu, X.; Xia, H.; Zhou, S.; Mei, Q. In Vitro and in Vivo Antitumor Activity of a Novel Ph-Activated Polymeric Drug Delivery System for Doxorubicin. *PLoS One* **2012**, *7*, e44116.
(43) Longhi, A.; Ferrari, S.; Bacci, G.; Specchia, S. Long-Term Follow-up of Patients with Doxorubicin-Induced Cardiac Toxicity after Chemotherapy for Osteosarcoma. *Anti-Cancer Drugs* **2007**, *18*, 737−744.
(44) Granados-Principal, S.; El-azem, N.; Pamplona, R.; Ramirez-Tortosa, C.; Pulido-Moran, M.; Vera-Ramirez, L.; Quiles, J. L.; Sanchez-Rovira, P.; Naudí, A.; Portero-Otin, M.; Perez-Lopez, P.; Ramirez-Tortosa, M. Hydroxytyrosol Ameliorates Oxidative Stress and Mitochondrial Dysfunction in Doxorubicin-Induced Cardiotoxicity in Rats with Breast Cancer. *Biochem. Pharmacol.* **2014**, *90*, 25−33.
(45) Hilmer, S. N.; Cogger, V. C.; Muller, M.; Le Couteur, D. G. The Hepatic Pharmacokinetics of Doxorubicin and Liposomal Doxorubicin. *Drug Metab. Dispos.* **2004**, *32*, 794−799.
(46) Ke, X.-Y.; Ng, V. W. L.; Gao, S.-J.; Tong, Y. W.; Hedrick, J. L.; Yang, Y. Y. Co-Delivery of Thioridazine and Doxorubicin Using Polymeric Micelles for Targeting Both Cancer Cells and Cancer Stem Cells. *Biomaterials* **2014**, *35*, 1096−1108.
(47) Yang, X.; Hong, H.; Grailer, J. J.; Rowland, I. J.; Javadi, A.; Hurley, S. A.; Xiao, Y.; Yang, Y.; Zhang, Y.; Nickles, R. J.; Cai, W.; Steeber, D. A.; Gong, S. cRGD-Functionalized, DOX-Conjugated, and ^{64}Cu-Labeled Superparamagnetic Iron Oxide Nanoparticles for Targeted Anticancer Drug Delivery and PET/MR Imaging. *Biomaterials* **2011**, *32*, 4151−4160.
(48) Xiong, H.; Du, S.; Ni, J.; Zhou, J.; Yao, J. Mitochondria and Nuclei Dual-Targeted Heterogeneous Hydroxyapatite Nanoparticles for Enhancing Therapeutic Efficacy of Doxorubicin. *Biomaterials* **2016**, *94*, 70−83.
(49) Li, L.; Fan, H.; Wang, L.; Jin, Z. Does Halloysite Behave Like an Inert Carrier for Doxorubicin? *RSC Adv.* **2016**, *6*, 54193−54201.
(50) Kostarelos, K.; Lacerda, L.; Pastorin, G.; Wu, W.; Wieckowski, S.; Luangsivilay, J.; Godefroy, S.; Pantarotto, D.; Briand, J.-P.; Muller, S.; Prato, M.; Bianco, A. Cellular Uptake of Functionalized Carbon Nanotubes Is Independent of Functional Group and Cell Type. *Nat. Nanotechnol.* **2007**, *2*, 108−113.
(51) Rong, R.; Xu, X.; Zhu, S.; Li, B.; Wang, X.; Tang, K. Facile Preparation of Homogeneous and Length Controllable Halloysite Nanotubes by Ultrasonic Scission and Uniform Viscosity Centrifugation. *Chem. Eng. J.* **2016**, *291*, 20−29.
(52) Veerabadran, N. G.; Price, R. R.; Lvov, Y. M. Clay Nanotubes for Encapsulation and Sustained Release of Drugs. *Nano* **2007**, *2*, 115−120.
(53) Yuan, P.; Southon, P. D.; Liu, Z.; Green, M. E.; Hook, J. M.; Antill, S. J.; Kepert, C. J. Functionalization of Halloysite Clay Nanotubes by Grafting with Γ-Aminopropyltriethoxysilane. *J. Phys. Chem. C* **2008**, *112*, 15742−15751.
(54) Kumar, A. V.; Varadaraj, M. C.; Lalitha, R. G.; Tharanathan, R. N. Low Molecular Weight Chitosans: Preparation with the Aid of Papain and Characterization. *Biochim. Biophys. Acta, Gen. Subj.* **2004**, *1670*, 137−146.
(55) Li, C.; Liu, J.; Qu, X.; Guo, B.; Yang, Z. Polymer-Modified Halloysite Composite Nanotubes. *J. Appl. Polym. Sci.* **2008**, *110*, 3638−3646.
(56) Mu, B.; Zhao, M.; Liu, P. Halloysite Nanotubes Grafted Hyperbranched (co) Polymers Via Surface-Initiated Self-Condensing Vinyl (co) Polymerization. *J. Nanopart. Res.* **2008**, *10*, 831−838.
(57) Liu, M.; Guo, B.; Du, M.; Cai, X.; Jia, D. Properties of Halloysite Nanotube−Epoxy Resin Hybrids and the Interfacial Reactions in the Systems. *Nanotechnology* **2007**, *18*, 455703.
(58) Sato, Y.; Yokoyama, A.; Shibata, K.-i.; Akimoto, Y.; Ogino, S.-I.; Nodasaka, Y.; Kohgo, T.; Tamura, K.; Akasaka, T.; Uo, M.; et al. Influence of Length on Cytotoxicity of Multi-Walled Carbon Nanotubes against Human Acute Monocytic Leukemia Cell Line THP-1 in Vitro and Subcutaneous Tissue of Rats in Vivo. *Mol. BioSyst.* **2005**, *1*, 176−182.
(59) Guan, S.; Liang, R.; Li, C.; Yan, D.; Wei, M.; Evans, D. G.; Duan, X. A Layered Drug Nanovehicle toward Targeted Cancer Imaging and Therapy. *J. Mater. Chem. B* **2016**, *4*, 1331−1336.
(60) Ritger, P. L.; Peppas, N. A. A Simple Equation for Description of Solute Release I. Fickian and Non-Fickian Release from Non-Swellable Devices in the Form of Slabs, Spheres, Cylinders or Discs. *J. Controlled Release* **1987**, *5*, 23−36.
(61) Liu, H.-Y.; Du, L.; Zhao, Y.-T.; Tian, W.-Q. In Vitro Hemocompatibility and Cytotoxicity Evaluation of Halloysite Nanotubes for Biomedical Application. *J. Nanomater.* **2015**, *2015*, 685323.
(62) Wang, S.; Konorev, E. A.; Kotamraju, S.; Joseph, J.; Kalivendi, S.; Kalyanaraman, B. Doxorubicin Induces Apoptosis in Normal and Tumor Cells Via Distinctly Different Mechanisms Intermediacy of H_2O_2-and p53-Dependent Pathways. *J. Biol. Chem.* **2004**, *279*, 25535−25543.
(63) Wang, X.; Song, Y.; Ren, J.; Qu, X. Knocking-Down Cyclin a 2 by Sirna Suppresses Apoptosis and Switches Differentiation Pathways in K562 Cells Upon Administration with Doxorubicin. *PLoS One* **2009**, *4*, e6665.
(64) Ma, Y.-C.; Wang, J.-X.; Tao, W.; Qian, H.-S.; Yang, X.-Z. Polyphosphoester-Based Nanoparticles with Viscous Flow Core Enhanced Therapeutic Efficacy by Improved Intracellular Drug Release. *ACS Appl. Mater. Interfaces* **2014**, *6*, 16174−16181.
(65) Ma, Y.-C.; Wang, J.-X.; Tao, W.; Sun, C.-Y.; Wang, Y.-C.; Li, D.-D.; Fan, F.; Qian, H.-S.; Yang, X.-Z. Redox-Responsive Polyphosphoester-Based Micellar Nanomedicines for Overriding Chemoresistance in Breast Cancer Cells. *ACS Appl. Mater. Interfaces* **2015**, *7*, 26315−26325.
(66) Mo, J.; He, L.; Ma, B.; Chen, T. Tailoring Particle Size of Mesoporous Silica Nanosystem to Antagonize Glioblastoma and Overcome Blood−Brain Barrier. *ACS Appl. Mater. Interfaces* **2016**, *8*, 6811−6825.
(67) Liu, Y.; Luo, Y.; Li, X.; Zheng, W.; Chen, T. Rational Design of Selenadiazole Derivatives to Antagonize Hyperglycemia-Induced Drug Resistance in Cancer Cells. *Chem. - Asian J.* **2015**, *10*, 642−652.
(68) Hamanaka, R. B.; Chandel, N. S. Mitochondrial Reactive Oxygen Species Regulate Cellular Signaling and Dictate Biological Outcomes. *Trends Biochem. Sci.* **2010**, *35*, 505−513.
(69) Pieczenik, S. R.; Neustadt, J. Mitochondrial Dysfunction and Molecular Pathways of Disease. *Exp. Mol. Pathol.* **2007**, *83*, 84−92.
(70) Bras, M.; Queenan, B.; Susin, S. Programmed Cell Death Via Mitochondria: Different Modes of Dying. *Biochemistry (Moscow)* **2005**, *70*, 231−239.

DOI: 10.1021/acsami.6b09074
ACS Appl. Mater. Interfaces 2016, 8, 26578−26590